

# Preliminary Investigation on Real-Time Induction Heating-Assisted Underwater Wet Welding

*A unique process that combines induction heating and flux cored arc wet welding to reduce cooling rates in real time was studied*

BY H. T. ZHANG, X. Y. DAI, J. C. FENG, AND L. L. HU

## ABSTRACT

A novel real-time induction heating-assisted underwater wet welding process was investigated. The addition of induction heating could reduce the cooling rate of the joint in underwater wet welding. The macro- and microstructures, mechanical properties such as tensile, impact, and bending properties, and Y-slit restraint testing were studied. The results showed the content of martensite (M) and upper bainite (BU) phases decreased, while the proeutectoid ferrite (PF) and acicular ferrite (AF) phases increased as the induction heating voltage increased. Mechanical properties of the joint were improved through addition of induction heating and fracture morphology with characteristic uniform dimples belonging to ductile fracture. The cracking ratio of Y-slit restraint testing was also decreased. Therefore, the susceptibility to cold cracking of the wet welding joint was improved.

## KEYWORDS

- Underwater Wet Welding • Induction Heating • Microstructure
- Property

## Introduction

Offshore development has accelerated in recent years owing to the fact that more than 50% of undeveloped petroleum deposits are located under the ocean. In the offshore industry and in underwater oil and gas pipelines, underwater welding is already a routine activity (Refs. 1, 2). The demand for underwater welding processes that can produce quality wet welds at greater depths, and on a variety of materials, will continue to increase (Ref. 3).

Underwater welding techniques can be classified as follows: wet welding, dry welding, and local cavity welding. Wet welding occurs directly in aqueous

environments with no mechanical barrier between water and welding arc. It was established that significant cost savings and simplicity of the process makes it possible to weld even the most geometrically complex structures; therefore, underwater wet welding is of increasing importance (Refs. 4, 5). The most commonly used wet welding techniques are shielded metal arc welding (SMAW) (Refs. 6, 7) and flux cored arc welding (FCAW). It was acknowledged that wet flux cored arc welding is promising in the future because of much higher production efficiency and applying in the automatic welding process (Refs. 8, 9).

In order to meet the requirements for offshore structures, high-strength

steel (yield strength over 350 MPa) is required. The strength of the steel used for offshore structures is a very important factor (Ref. 10). Unfortunately, high-strength low-alloy (HSLA) steels usually have carbon equivalents greater than 0.4% and show poorer weldability. At the same time, an aqueous environment produces a lot of disadvantageous effects (Ref. 11), such as the cooling effect of the surrounding water, loss of alloying elements, and considerable amounts of diffusible hydrogen (Ref. 12). The cooling rate in wet welding is much higher than in dry welding, such as in the temperature range from 800° to 500°C, it can rise sharply from 56° to 415°C/s (Ref. 4). This causes brittle weld microstructures and high amounts of hydrogen porosity, which can be causes of crack formation. Susceptibility to cold cracking is the main problem in welding of HSLA steels and fabrication of dissimilar joints.

Many researchers have attempted to use special methods to avoid these adverse effects. Many studies utilized the temper bead technique (Refs. 13–15). A full welding procedure qualification without cracking has been completed for a base plate having a carbon equivalent of 0.44. However, this method is only suitable for repair of underwater structures, which limits its application. In addition, insulating materials (Refs. 16, 17) were used to control cooling rates in underwater wet welds. The research, taking into account the insulating material, developed an empirical relationship to predict the optimized cooling rates and

H. T. ZHANG (hitzht@163.com), X. Y. DAI (hitdxy29@gmail.com), J. C. FENG, and L. L. Hu are with the State Key Laboratory of Advanced Welding and Joining, Harbin Institute of Technology, Harbin, China; Shandong Provincial Key Laboratory of Special Welding Technology, Harbin Institute of Technology at Weihai, Weihai, China.

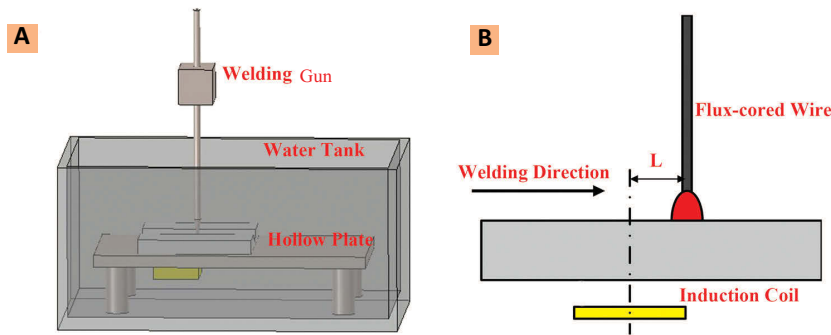


Fig. 1 — Schematic of the assembled device.

Table 1 — Chemical Composition of Q460 (not more than wt-%)

Base Metal	C	Si	Mn	V	Ti	Cr	Ni	Cu	Mo
Q460	0.2	0.6	1.8	0.2	0.2	0.3	0.8	0.55	0.2

times for underwater wet welds. Fox (Ref. 18) and Pope (Ref. 19) investigated the water temperature and water depth influences on hydrogen-induced cracking, microstructure, and mechanical properties in underwater wet welding, and the importance of water temperature and water depth, quenching, and diffusible hydrogen levels in underwater wet welding have been demonstrated. Postweld heat treatment (PWHT) is frequently used to reduce hardened structure and allow hydrogen to diffuse away from the weld metal and heat-affected zone (HAZ) (Ref. 20). Szelagowski (Refs. 21, 22) used a  $H_2-O_2$  cutting torch and an underwater high-velocity oxyfuel (UW-HVOF) thermal spraying device to serve as PWHT on wet welds. The hydrogen content of the weld metal was reduced and the bend testing result showed a higher plastic property. However, the control of heat input could not be accurate and efficient.

In this paper, a novel real-time induction heating-assisted underwater wet welding process was employed for the first time. Induction heating could reduce the cooling rates of the joint in underwater wet welding, especially the  $t_{8/5}$  (the cooling time range from  $800^\circ$  to  $500^\circ C$ ) was extended. According to welding CCT diagrams, it reduced the hardened and brittle transformation products. That is, the content of martensite (M) and upper bainite (BU) phases decreased as the content of proeutectoid ferrite (PF) and acicular ferrite (AF) phases increased. Therefore, the purpose of this work was to develop

a novel method to obtain an excellent quality underwater wet welding joint.

## Experimental Procedure

Q460 steel (equivalent to Gr. 65 steel of AST-USA or E460DD steel of 630-ISO) delivered as rolled sections with the dimensions of  $300 \times 90 \times 8$  mm was used as the base metal. The single-V weld groove had a 60-deg included angle with a 2-mm root face and 1.5-mm root opening. The chemical composition of the sheets is shown in Table 1. Prior to welding, the oxide layers on the surfaces of the plates were removed by stainless steel wire brushing and the weld zone was degreased using acetone. The as-received plates were welded together with the gas tungsten arc (GTA) and flux cored arc (FCA) welding processes. GTAW was used for the root pass to fix the plates with 100-A DC and 20 V in air. Underwater wet FCAW was used for the fill passes and optimized welding parameters are listed in Table 2.  $TiO_2-CaF_2$  type flux-cored wire with a diameter of 1.2 mm produced by Paton Welding Institute was chosen.

A schematic of the assembled device is shown in Fig. 1. The device could be divided into two sections: underwater welding system and induction heating system. The water in the tank was stationary and the water depth was 300 mm. A circular, 60-mm-diameter induction coil was installed behind the welding gun in the welding direction and below the plates in the vertical direction. The welding gun and induction coil were fixed together

and moved at the same speed. The parameter  $L$  — defined as the distance between the center of the coil and the center of the welding gun — was constant. The induction heating source had an output voltage of 70–550 V. Changing the induction heating voltage meant changing the output power due to the constant system impedance. Type-K thermocouples with shielding were placed at different locations from the edge of the weld groove to measure the temperature profile. Four-channel data loggers were used to record the temperature measurements with a sampling frequency of 25 Hz. The measurement method of the HAZ temperature field was as follows: weld HAZ without installed thermocouples was first identified to be about 2.0 mm from the weld interface, then the thermocouples located at or near 2.0 mm from the weld interface were identified as that representing the HAZ thermal cycle (Ref. 23).

A CCD camera with a frame rate of 2000 frames/s was used to record images of the arc behavior in order to investigate the effect of the induction magnetic field. The metallographic specimens of a typical cross section were prepared vertical to the weld joint and all specimens were polished with SiC papers up to grit 1000, and ultrasonically cleaned with acetone to remove oil and other contaminants from the specimen surfaces. Etching with 5% nitric acid and alcohol solution for 3–4 s was used to reveal the weld beam. The macro- and microstructure fracture morphology were observed by optical microscopy (OM) and scanning electron microscopy (SEM), respectively. Mechanical property tests such as tensile testing, impact testing, and bend testing were investigated to build an empirical relationship between induction heating voltages and mechanical properties.

## Results and Discussion

### Welding Process Stability

A welding arc is an electric discharge between two electrodes and a heated and ionized gas, called plasma (Ref. 24). Therefore, the arc stability could be adversely affected as a result of the magnetic field of induction heating and eddy current. Figure 2 shows the captured images of arc

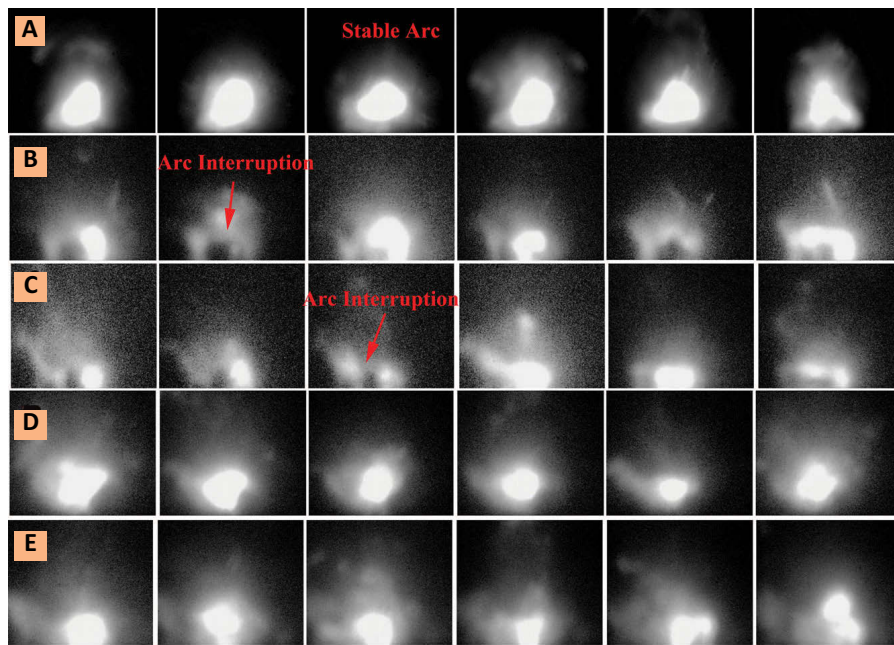


Fig. 2 — Captured images of arc shape: A — Without induction heating; B — L = 5 mm, 250 V; C — L = 5 mm, 450 V; D — L = 20 mm, 250 V; E — L = 20 mm, 450 V.

Table 2 — Optimized Welding Parameters

Welding Voltage (V)	Welding Current (A)	Welding Speed (mm/min)	Water Depth (mm)
26	160	145	300

shape with parameter L and induction heating voltages. Due to optimum parameters and flux-cored wire, the welding arc was steady during the underwater welding process without induction heating (Fig. 2A). While the induction coil was installed, the arc stability was reduced. It was observed that the parameter L played a major role in arc stability. When the parameter L was 5 mm, the welding arc was extremely unstable and even arc interruption appeared in Fig. 3A. At the same time, when parameter L was increased to 20 mm, the welding arc shape was stable. Therefore, a continuous and uniform weld could be observed in Fig. 3B. Welding discontinuities, such as incomplete fusion and undercut, were not found. In addition, the induction heating voltage affected arc stability and the arc stability decreased with increased voltage. To investigate the influence of voltage on the joint, the parameter L was fixed as 20 mm in the subsequent experiments.

**Cross-Section Macrographs**

Q460 sheets were underwater weld-

ed at a fixed welding parameter (Table 2) and at various induction heating voltages ranging from 250 to 450 V in order to clarify the effect of induction voltage on weld penetration. Cross-sectional macrographs of the joints with different voltages are shown in Fig. 4. According to the results, weld penetration and HAZ increased with the increasing voltage. As was known, the width of the HAZ depended primarily on heat input. The heat input was the sum of welding heat input and induction heating. Therefore, the effect of induction heating was equal to increasing the welding heat input. In addition, the induction heating made the temperature field of the weld zone relatively more uniform.

**Microstructure Characteristics of the Joints**

The HAZ for Q460 delivered as rolled sections mainly consisted of two distinct zones: coarse-grained HAZ (CGHAZ) and fine-grained HAZ (FGHAZ). Typical HAZ temperature vs. time profiles during the underwater wet welding are shown in Fig. 5. Ac-

ording to the results, the cooling rate in wet welding was extremely higher than in air welding. For instance, the cooling rate of the temperature range from 800° to 500°C could rise sharply to 100°C/s, which was more than the critical cooling speed of martensite formation.

Figure 6 showed the optical microstructure of the weld zone with various induction heating voltages. Based on the theory of welding metallurgy, as the austenite phase was cooled down from high temperature, ferrite nucleated at the grain boundary at 770°–680° and then grew inward. This ferrite was proeutectoid ferrite (PF), which is also called grain boundary ferrite (GBF). When the temperature dropped to 500°, the transformation of acicular ferrite (AF) occurred. The acicular ferrite phase was a desirable phase because of the excellent plasticity and toughness characteristics (Ref. 25). As the cooling rate increased, the transformation product changed to bainite and martensite phase and reduced the mechanical properties. The microstructure of the weld zone in air welding was composed of proeutectoid ferrite and acicular ferrite phase. As was mentioned previously, the acicular ferrite phase had excellent plasticity and toughness, due to the interlocking nature of the acicular ferrite and the fine granular size. Therefore, the mechanical properties were satisfactory. Compared to air welding, the microstructure of underwater welding was a mixture of lath martensite, upper bainite, and proeutectoid ferrite — Fig. 6A. The bainite sheaf and martensite lath nucleated and grew from prior austenite granular boundaries. The formation of lath martensite and upper bainite were detrimental to the weld properties, owing to the easy crack propagation paths. As the induction heating voltages increased (Fig. 6 B–D), the volume fraction of lath martensite and upper bainite decreased with ferrite phases increasing. Moreover, the lath martensite and upper bainite phase disappeared as the voltage reached 350 V. The transformation product (Fig. 6C) could change from upper bainite and lath martensite to acicular ferrite and proeutectoid ferrite. Therefore, the microstructure of the weld metal was

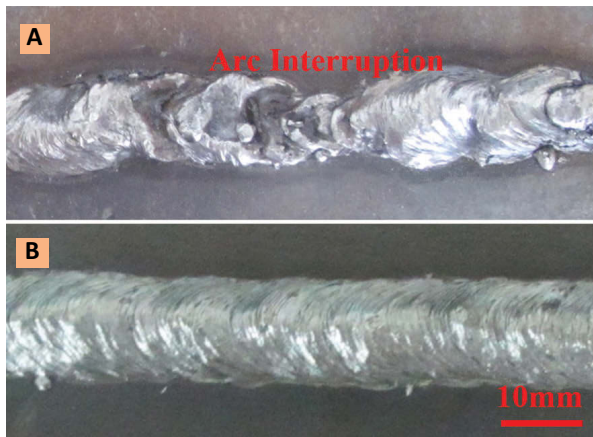


Fig. 3 — Weld appearances: A —  $L = 5$  mm, 250 V; B —  $L = 20$  mm, 250 V.

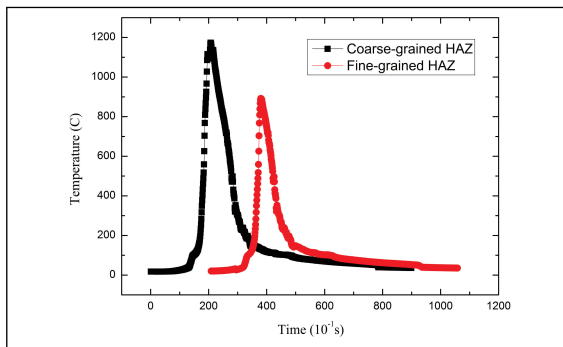


Fig. 5 — Measured temperature vs. time curves of underwater wet welding without induction heating.

similar to air weld, the only difference was the morphology of the proeutectoid ferrite. Increased acicular ferrite content in the microstructure improved cracking resistance, while upper bainite and lath martensite deteriorated the mechanical properties of the joint. The dimension of the proeutectoid ferrite was increased with the increase in the voltage. As the voltage was 450 V (Fig. 6D), the morphology of the proeutectoid ferrite was coarsening and a ferrite side plate (FSP) was found. Because of the limited output voltage of the induction heating system, the induction heating was higher than 450 V, and the microstructural evolution and mechanism are to be investigated in the future.

To understand the mechanism of weld microstructural evolution, temperature vs. time profiles of different induction heating voltages without being subjected to welding are shown in Fig. 7. The parameters of  $t_{8/5}$ , for a given

hardenability steel, determined the hardenability of the transformation products, which should be taken into consideration to investigate the effect on susceptibility to hydrogen-induced cracking. The data of temperature vs. time curves are shown in Table 3. As the induction heating voltage was 250 V, the  $T_{max}$  reached 412°C. Therefore, the microstructure of Fig. 6B was similar to that shown in Fig. 6A because the  $t_{8/5}$  determined the transformation products. As the induction heating voltage was 350 V, the  $T_{max}$  was increased to 609°C and the  $t_{8/5}$  was prolonged at the same time. Therefore, the transformation products changed from upper bainite and lath martensite to acicular ferrite and proeutectoid ferrite due to the fact  $t_{8/5}$  was prolonged. A comparison of temperature curves of 0 and 450 V is shown in Fig. 8. It could be seen that the prolongation of  $t_{8/5}$  was extremely obvious. That's the reason for the evolution of the microstructure of the weld metal.

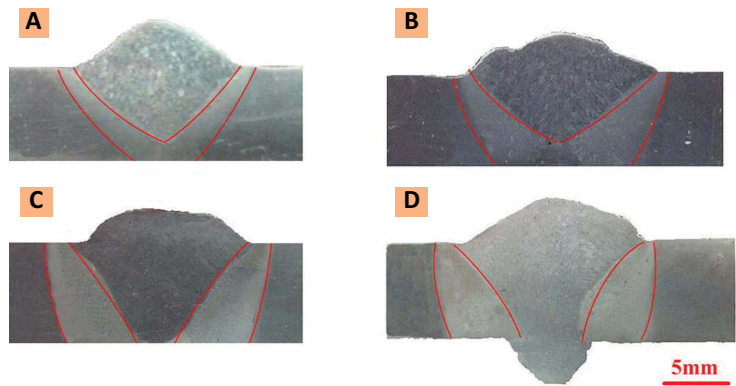


Fig. 4 — Cross-sectional macrograph of the joints: A — 0 V; B — 250 V; C — 350 V; D — 450 V.

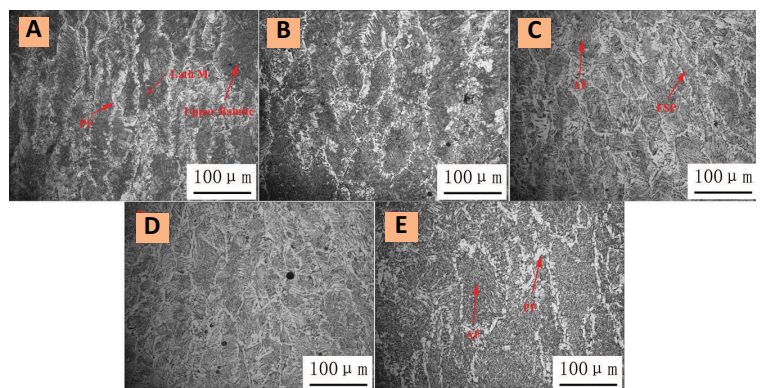


Fig. 6 — The optical microstructure of the weld zone with various induction heating voltages: A — 0 V; B — 250 V; C — 350 V; D — 450 V; E — in air.

Figure 9 showed the optical microstructure of the partially melted zone with and without induction heating. The red line was the weld interface of the joint. It could be seen that lath martensite (M) and coarsening Widmanstätten (W) structure was predominant in the coarse-grained HAZ in Fig. 9A. The ferrite phase precipitated first in the coarse-grained austenite grain boundary, and then grew into the austenite in the form of reticular structure (also called W structure), resulting in splitting the matrix structure, even generating the crack. And the lath martensite composed of vast coarse lath was beneficial for crack initiation and propagation. Therefore, the mechanical properties of the joint were decreased. However, as the voltage was 350 V, granular bainite was predominant and grain coarsening was relieved. Thus, the tendency to crack was decreased, and the mechanical properties of the joint were increased.

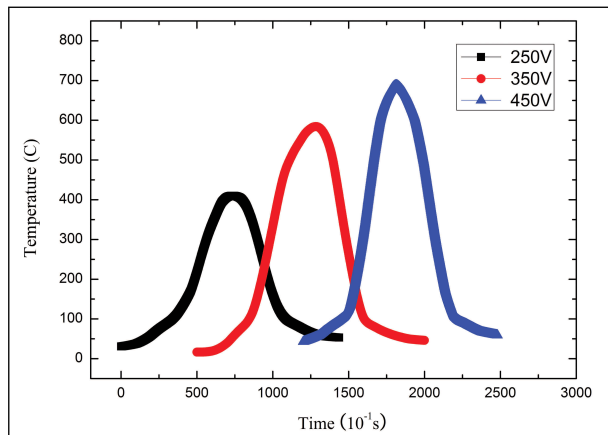


Fig. 7 — Temperature vs. time profiles of different induction heating voltages without being subjected to welding.

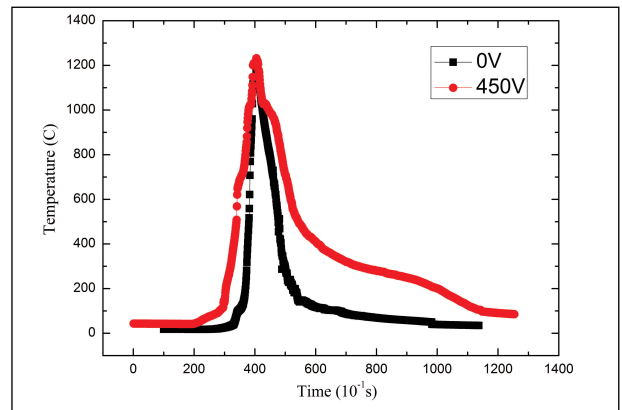


Fig. 8 — Compared temperature vs. time curves during underwater wet welding with various induction heating voltages.

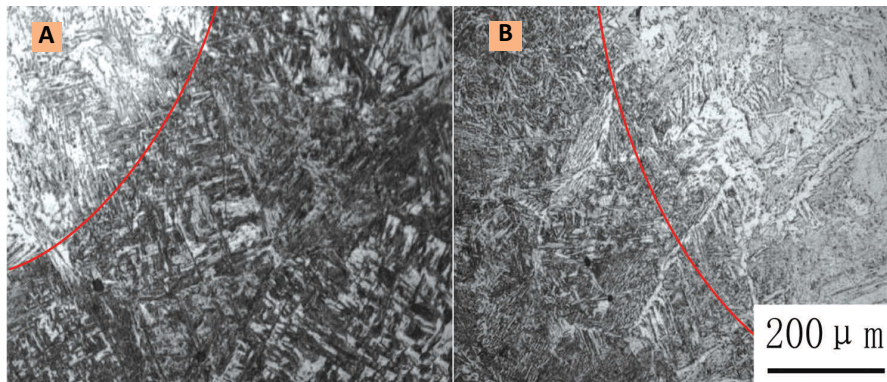


Fig. 9 — The optical microstructure of the weld interface: A — 0 V; B — 350 V.

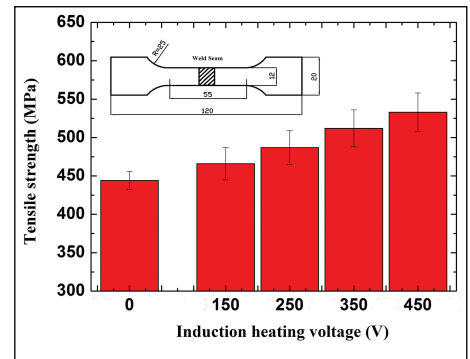


Fig. 10 — Tensile strength vs. induction heating voltage curves.

Table 3 — The Data of Temperature vs. Time Curves

Induction Heating Voltages (V)	T <sub>max</sub> (°C)	t <sub>8/5</sub> (s)
250	412	0
350	609	24
450	712	35

## Mechanical Properties

### Tensile Testing and Fracture Morphology

Five prepared tensile specimens from each joint were performed using a fully computerized tensile testing machine with a loading rate of 1 mm/min at room temperature to evaluate the influence of various induction heating voltages on the mechanical properties of the joint. The geometry of the tensile specimens and tensile strength vs. voltage curves are shown in Fig. 10. The thickness of the specimen was 4 mm. The tensile strength

of specimens without induction heating was 444 MPa, about 82.2% of the base metal (540 MPa). The tensile property increased gradually with increasing voltages. As the voltage was 450 V, the tensile strength reached 532 MPa, about 98.5%, and all the joints fractured roughly in the HAZ. Joint efficiency increased from 82.2 to 98.5%.

In order to observe the fracture mechanism, SEM was carried out to analyze the fracture morphology. Figure 11 shows the typical fracture surface of specimens with different voltages. It can be seen that a quasi-cleavage fracture mode was dominant in Fig. 11A, due to plenty of cleavage plane appear-

ance. The size of the cleavage plane was related to the crack path. The large cleavage planes demonstrated very low crack propagation energy, while the small cleavage plane exhibited higher crack propagation energy (Ref. 26). The formation of lath martensite and W structure in the HAZ was detrimental to tensile property due to the easy crack propagation paths. Once the crack occurred during the tensile test, it could propagate along the paths of lath martensite and W structure rapidly. Therefore, tensile strength without induction heating was the lowest. The dimple characteristics became predominant as the voltage was increased in Fig. 11B–D. Cleavage planes were in small proportion while dimples were in large proportion, as shown in Fig. 11B. Therefore, the fracture morphology had the characteristic of ductile fracture. While the voltage was above 350 V, the cleavage planes disappeared, instead of uniform dimples, which was the typical feature of ductility. Nonmetallic inclu-

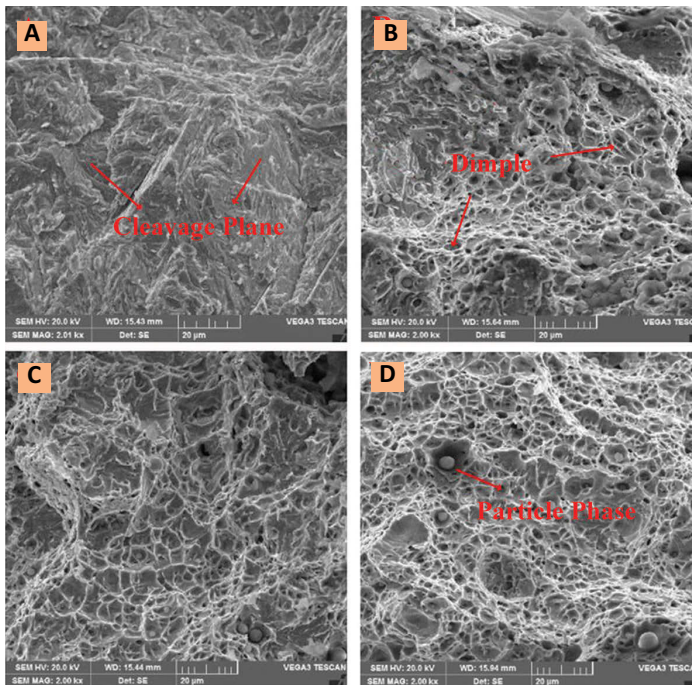


Fig. 11 — SEM images of the fractured surface of specimens with various voltages: A — 0 V; B — 250 V; C — 350 V; D — 450 V.

sions phase were disorderly distributed in the inter-tear edges. Hence, tensile property of the joints improved to about 98.9% of the base metal.

## Impact Testing and Fracture Morphology

Charpy V-notch impact tests were conducted at 20°C on an instrumented drop weight impact tester. The specimens were extracted in the weld's perpendicular direction from the middle thickness of the as-welded specimen with notches positioned at the center of the weld metal. The impact energy of the joints was the average of five specimens. The geometry of the Charpy impact V-notch specimens and impact energy vs. induction heating voltage curves are shown in Fig. 12. The thickness of the specimen was 10 mm. The impact energy value of specimens without induction heating was 36 J. As the voltage increased, the impact energy increased consistently. Finally, as the voltage was 350 V, the impact energy could reach 68 J. The results suggested that induction heating could increase the impact properties and the toughness of the joint.

For the purpose of observing the fracture mechanism, SEM was used to

analyze the fracture morphology. Figure 13 shows the SEM micrographs of impact fracture surface morphologies for different voltages. It can be seen that a cleavage fracture mode is dominant in Fig. 13A, due to a network of cleavage steps known as a river pattern. Cleavage was a low-energy fracture that propagated along well-defined low-index crystallographic planes known as cleavage planes. The branches of the river pattern joined in the direction of crack propagation. Meanwhile, the formation of lath martensite and upper bainite was adverse to the toughness of the joint due to the easy crack propagation paths. Once the crack occurred, it rapidly propagated in a straight line along the lath martensite and upper bainite paths. Therefore, the impact energy value without induction heating was the lowest. However, the dimples started to appear and were present in small proportion when the voltage was at 250 V in Fig. 13B. Feather markings, which are a fan-shaped array of very fine cleavage steps on a large cleavage facet, are

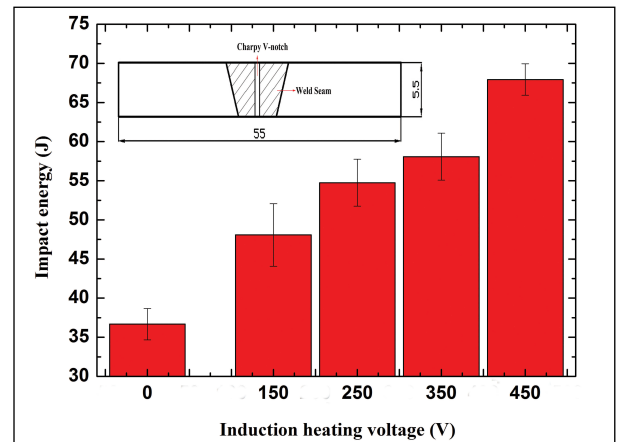


Fig. 12 — Impact energy vs. induction heating voltage curves.

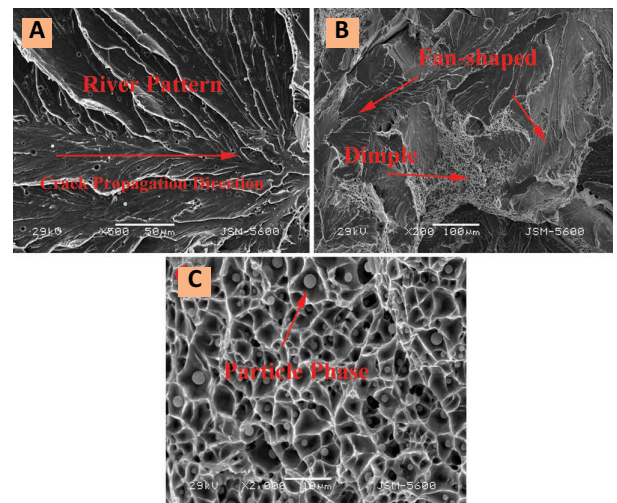


Fig. 13 — SEM images of the fractured surface of specimens with various voltages: A — 0 V; B — 250 V; C — 350 V.

present in large proportion. The apex of the fan points back to the fracture origin. While the voltage was 350 V, the cleavage planes disappeared, instead of uniform dimples, which was the characteristic of ductile fracture. Some nonmetallic inclusions phase showed in a disorderly distribution and were surrounded by the inter-tear edges. The reason for these results was that the acicular ferrite acted as the crack arrester and increased the crack propagation energy. Therefore, the impact property of the joints was greatly improved from 36 to 68 J.

## Bend Testing

Longitudinal three-point bend tests were conducted to measure the bending ductility at room temperature. The an-

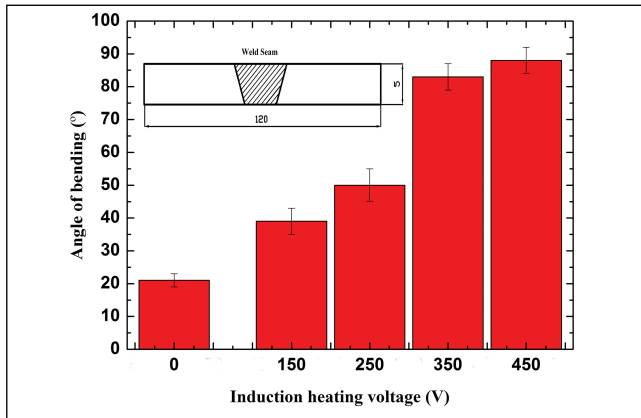


Fig. 14 — Angle of bending vs. induction heating voltage curves.

gle of bending for the joints was the average of three specimens. The geometry of the specimens and angle of bending vs. induction heating voltage curves are shown in Fig. 14. The thickness of the specimen was 5 mm. According to the results, the angle of bending values of specimens without induction heating was 21 deg, which indicated ductility was very low. At the same time, the angle of bending values increased rapidly with increasing voltages. Finally, as the voltage was 450 V, the angle of bending values reached 88 deg. The results suggested joint ductility had been increased.

### Y-Slit Restraint Testing

Because of the high quenching rate caused by the water environment and because large quantities of hydrogen are present, hydrogen cracking is one of the most severe problems in the underwater welding of steel (Ref. 27). The cracking tests were carried out using a Y-slit restraint test so that the intensity of the restraint could be related to actual fabricating conditions. The geometry of specimens subjected to Y-slit restraint testing and the cracking ratio used as a measure of the cracking susceptibility are shown in Fig. 15. This is a ratio of the height from the root to the tip of the crack vs. the height from the root to the surface of the weld metal.

The cracking ratio vs. induction heating voltage curves are shown in Fig. 16. The carbon equivalent value of Q460 steel was 0.6, which indicated the steel was particularly sensitive to cracking, especially in underwater welding.

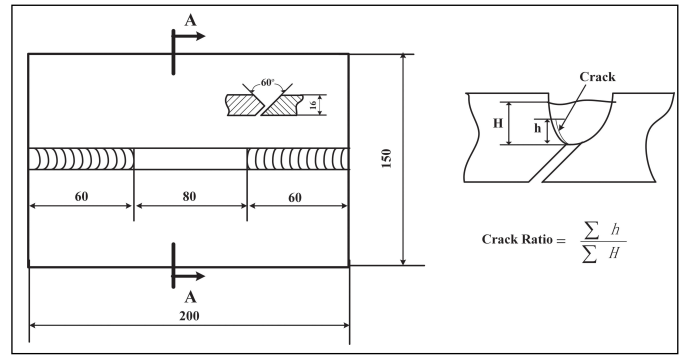


Fig. 15 — Schematic of Y-slit self-restrained cracking test (mm).

Therefore, the cracking ratio of specimens without induction heating was

82%. However, as the voltage reached 150 and 250 V, the cracking ratio decreased rapidly to 45% and 22%, respectively. Finally, when the voltage was above 350 V, the cracking ratio reached about 10%. Typical weld cross sections with various induction heating voltages are shown in Fig. 17. According to the results, induction heating could reduce the cooling rate; therefore, the cracking susceptibility was decreased.

### Microhardness Profile

Vickers microhardness measurement across the fusion zone was carried out with a load of 100 g and load time of 10 s. Results of hardness measurements are shown in Fig. 18. The microhardness distribution indicated the microstructural characteristics of the joint. Increased hardness values of the weld metal confirmed these microstructural changes. The location of the HAZ was determined by metallographic observation and the hardness of the HAZ was higher than that of the weld metal. The HAZ and weld metal hardness decreased with increased induction heating voltage. The maximum hardness of HAZ without induction heating was 425 HV, which was much harder than that with 250 and 450 V. The hardness values of the weld zone with 250 and 450 V were relatively uniform because the lath martensite and upper bainite content decreased while the acicular ferrite and proeutectoid ferrite increased. The results indicated induction heating had a significant effect on the maximum hardness. The microhardness profile

across the weld indicated the microstructural characteristics of the joint. Induction heating made the joint microhardness relatively more uniform.

### Conclusion

- 1) A novel real-time induction heating-assisted underwater wet welding process was employed. The addition of induction heating could reduce the cooling rate of the joint in water environment to improve the microstructural and mechanical properties of the joint.
- 2) Arc stability was reduced with the addition of induction heating. The parameter L played a major role in arc stability. As the parameter L increased to 20 mm, the welding arc shape was stable. A continuous and uniform weld joint could be observed.
- 3) The content of martensite (M) and upper bainite (BU) phases decreased while the proeutectoid ferrite (PF) and acicular ferrite (AF) phases increased as the induction heating voltage increased. Mechanical properties, such as tensile, impact, and bending properties, increased as the induction heating voltages increased.
- 4) Cracking was examined via a Y-slit restraint test. The addition of induction heating could decrease the cracking ratio from 82 to 10%. Therefore, induction heating could make cracking susceptibility decrease.

### References

1. Brown, R. T., and Masubuchi, K. 1975. Fundamental research on underwater welding. *Welding Journal* 54(6): 178-s to 188-s.
2. Rowe, M., and Liu, S. 2001. Recent developments in underwater wet welding. *Science and Technology of Welding and Join-*

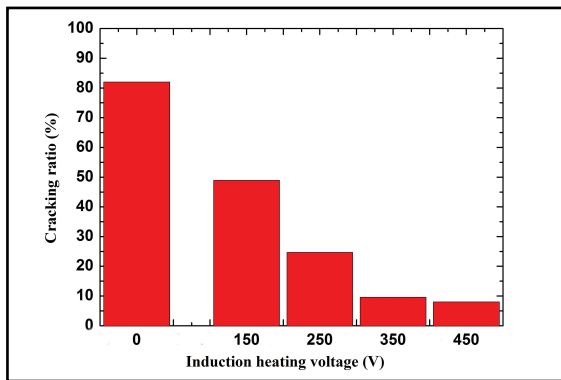


Fig. 16 — Cracking ratio vs. induction heating voltage curves.

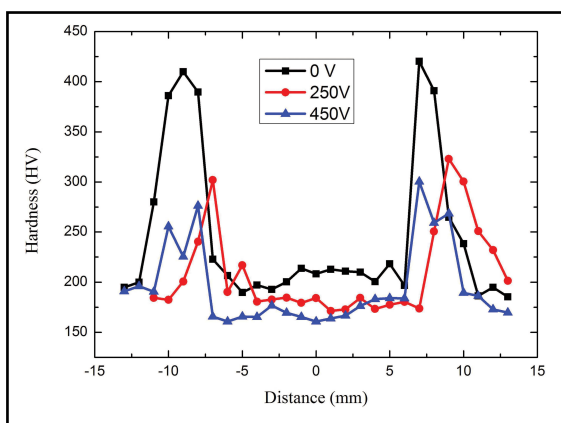


Fig. 18 — Hardness distribution along the joint.

ing 6: 387–396.

3. Łabanowski, J. 2011. Development of underwater welding techniques. *Welding International* 25: 933–937.

4. Łabanowski, J., and Fydrych, D. Rogalski, G. 2008. Underwater welding — A review. *Advances in Materials Science* 8: 11–22.

5. Ibarra, S. J., Reynolds, T. J., and Gabriel, G. 1996. Amoco Trinidad selects wet welding repair option. *Proceedings of the International Conference on Offshore Mechanics and Arctic Engineering* 3: 109–112.

6. Yara, H., Makishi, Y., Kikuta, Y., and Matsuda, F. 1987. Mechanical and metallurgical properties of an experimental covered electrode for wet underwater welding. *Welding International* 1: 835–839.

7. Liu, S., Olson, D. L., and Ibarra, S. J. 1995. Designing shielded metal arc consumables for underwater wet welding in offshore applications. *Journal of Offshore Mechanics and Arctic Engineering* 117: 212–220.

8. Kononenko, V. Y. 1996. Mechanised welding with self-shielding, flux-cored wires for repairing hydraulic installations and vessels in water. *Welding International* 10: 994–997.

9. Jia, C. B., Zhang, T., Maksimov, S. Y., and Yuan, X. 2013. Spectroscopic analysis of the arc plasma of underwater wet flux-

cored arc welding. *Journal of Materials Processing Technology* 213: 1370–1377.

10. Maksimov, Y. S. 2010. Underwater arc welding of higher strength low-alloy steels. *Welding International* 24: 449–454.

11. Skorupa, A., and Bal, M. 1996. The effect of aqueous environments on the quality of underwater-welded joints. *Welding International* 10: 95–98.

12. Pope, A. M., Medeiros, R. C., and Liu, S. 1995. Solidification of underwater wet welds. *Proceedings of the International Conference on Offshore Mechanics and Arctic Engineering* 3: 517–521.

13. Grubbs C. E. 1993. Underwater wet welding (a state of the art report). *Proceeding of the International Conference on Offshore Mechanics and Arctic Engineering* 3: 111–118.

14. Grubbs, C. E., Reynolds, T. J. 1998. State-of-the-art underwater wet welding. *World Oil* 219: 79s.

15. Grubbs, C.E., and Reynolds, T. J. 1998. Underwater welding: Seeking high quality at greater depths. *Welding Journal* 77(9): 35–39.

16. Tsai, C. L., and Masubuchi, K. 1979. Mechanisms of rapid cooling in underwater welding. *Applied Ocean Research* 1: 99–110.

17. Hasui, A., and Suga, Y. 1980. On cooling of underwater welds. *Transactions of the Japan Welding Society* 11: 21–28.

18. Fox, A. G., Johnson, R. L., and Dill, J. F. 1998. Effect of water temperature on the underwater wet weldability of ASTM A516 grade 70 steel. *Proceedings of the 1998 17th International Conference on Offshore Mechanics and Arctic Engineering*.

19. Pope, A. M., Teixeira, J. C. G. 1997. Influence of water depth on microstructure and mechanical properties of wet welds. *Proceedings of the International Conference on Offshore Mechanics and Arctic Engineering* 3: 13–19.

20. Szelagowski, P., and Ibarra, S. 1992. In-situ post-weld heat treatment of wet welds. Offshore Technology Conference, Houston, Tex.

21. Ohliger, A., and Szelagowski, P. 1992. Thermal spraying in wet environment. *The Proceedings of the 2nd (1992) International Offshore and Polar Engineering Conference* 4: 220.

22. Ohliger, A., Szelagowski, P., and Schafstall, H. 1991. *Thermal Spraying: Recent Developments for Underwater Application* 3: 193.

23. Silwal, B., Li, L., Deceuster, A., and Griffiths, B. 2013. Effect of postweld heat treatment on the toughness of heat-affected zone for grade 91 steel. *Welding Journal* 92(1): 80-s to 87-s.

24. *Welding Handbook*. 8th edition. 1991. Ed. R. L. O'Brien. Miami, Fla.: American Welding Society.

25. Zachrisson, J., Borjesson, J., and Karlsson, L. 2013. Role of inclusions in formation of high strength steel weld metal microstructures. *Science and Technology of Welding and Joining* 18: 603–609.

26. Hu, J., Du, L. X., Wang, J. J., Gao, C., and Gao, R. 2013. Effect of welding heat input on microstructures and toughness in simulated CGHAZ of V-N high strength steel. *Materials Science & Engineering A* 577: 16–168.

27. Ozaki, H., Naiman, J., and Masubuchi, K. 1977. A study of hydrogen cracking in underwater steel welds. *Welding Journal* 56(8): 231-s to 237-s.

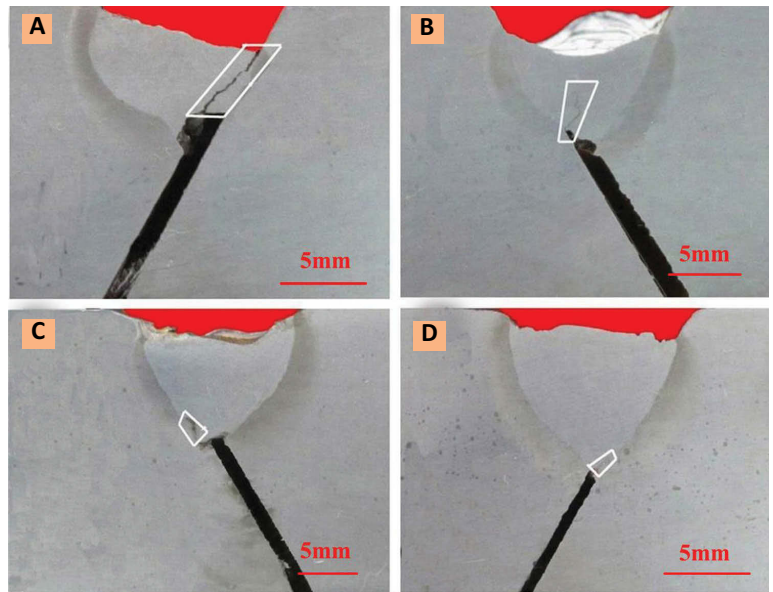


Fig. 17 — Typical underwater weld cross sections with various induction heating voltages: A — 0 V; B — 150 V; C — 250 V; D — 350 V.